Photoacoustics 41 (2025) 100672

Contents lists available at ScienceDirect

Photoacoustics

journal homepage: www.elsevier.com/locate/pacs

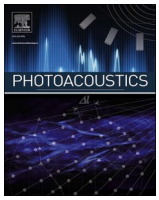

Improved T-shaped quartz tuning fork with isosceles-trapezoidal grooves optimized for quartz-enhanced photoacoustic spectroscopy

Feihu Fang [a,1], Runqiu Wang [b,1], Dongfang Shao [a], Yi Wang [a], Yilü Tao [a], Shengshou Lin [a], Yufei Ma [b,*], Jinxing Liang [a,*]

[a] Key Laboratory of Micro-Inertial Instrument and Advanced Navigation Technology Ministry of Education, School of Instrument Science and Engineering, Southeast University, Nanjing 210096, China
[b] National Key Laboratory of Laser Spatial Information, Harbin Institute of Technology, Harbin 150001, China

ARTICLE INFO

Keywords:
Quartz tuning fork
Quartz-enhanced photoacoustic spectroscopy
Isosceles-trapezoidal grooves
Gas sensing

ABSTRACT

The quartz tuning fork (QTF) being the acoustic-electrical conversion element for quartz-enhanced photoacoustic spectroscopy (QEPAS) system directly affects the detection sensitivity. However, the low electromechanical conversion efficiency characteristic of standard QTF limits the further enhancement of the system. Therefore, the optimized design for QTF is becoming an important approach to improve the performance of QEPAS. In this work, 9 kHz T-shaped QTFs with isosceles-trapezoidal grooves are firstly applied to gas sensing experiments. Four types of 9 kHz QTFs are fabricated and applied to gas detection experiments. Simulation results reveal QTFs with isosceles-trapezoidal grooves are conducive to optimizing the stress distribution and enhancing electro-mechanical conversion efficiency. The results of the gas sensing experiment (acetylene C_2H_2) indicate that the signal peak and signal-to-noise ratio values of T-shaped QTF with positive isosceles-trapezoidal grooves can reach 1.44 and 1.85 times greater than the normal QTF with rectangular cross-section prongs.

1. Introduction

Optical sensing technologies are widely adopted in many fields [1–10]. Laser spectroscopy based methods have the advantages of high sensitivity and non-invasive measurement [11–25]. As a type of laser absorption spectroscopy technology, Quartz-enhanced photoacoustic spectroscopy (QEPAS) has developed rapidly in gas sensing due to its excellent identification characteristics and high detection sensitivity [26,27], stemming from the fingerprint absorption characteristics of molecules. Tittel's team first proposed the QEPAS [28], in which the QTF replacing the microphone acts as acoustic-electric conversion. Compared with the microphone applied for conventional photoacoustic spectroscopy (PAS), the QTF has a higher quality factor, narrower response frequency bandwidth, and smaller geometry [29–34]. Therefore, the application of QTFs is beneficial in decreasing the background noise while enhancing the signal amplification of gas sensing [35–37].

The QTF, serving as the acoustic-electrical conversion element in QEPAS, converts periodic sound waves into surface electric charges. Specifically, periodic sound waves appeared at prongs' spacing push prongs to vibrate in anti-symmetrical mode, and electric charges can be collected in the prong surfaces periodically due to the positive piezoelectric effect [30,38]. In the development of QEPAS technology, standard QTFs have been widely used and demonstrated to be efficient [39–42]. However, the high resonance frequency and narrow prong spacing result in weak detection capability and increased optical noise, thereby further limiting the sensing performance of QEPAS [43]. Consequently, optimizing QTF design has become an important approach to improve the sensing performances of QEPAS technology.

In QEPAS, the frequency of QTFs directly affects the energy accumulation time of the system [44]. Compared to the standard QTFs with a high frequency of 32.768 kHz, QTFs with a low resonance frequency were designed to enhance the energy accumulation time and the detection signal [45–53]. Generally, the frequency and quality factor can be adapted by changing the dimensions of QTF. Up to now, there are two optimized prong structures widely used to improve sensor performances. The first optimized structure is the T-shaped prong [43,54–59], which can be regarded as adding an extra mass to the free end of the pong. The T-shaped prong structure can increase the vibration

* Corresponding authors.
E-mail addresses: mayufei@hit.edu.cn (Y. Ma), j-liang@seu.edu.cn (J. Liang).
[1] These authors contributed equally to this work.

https://doi.org/10.1016/j.pacs.2024.100672
Received 4 October 2024; Received in revised form 12 November 2024; Accepted 25 November 2024
Available online 26 November 2024

amplitude and improve the quality factor. Another optimized structure is carving rectangular grooves on the upper and lower surfaces of prongs [54,60,61]. In this work, the QTF vibrates along the X-axis, which corresponds to the electric axis of quartz crystal, and the grooves are carved in the upper and lower surfaces of the pongs. Compared with normal rectangular cross-section prongs, prongs with rectangular grooves benefit from enhancing the electric field intensity in the X-axis (the vibration direction of the QTF and the electric axis of quartz crystal) and improving the efficiency of electromechanical conversion.

For QTF, larger stresses lead to more surface electric charges, and stresses are the largest in the prong bottom region [43]. Therefore, making full use of the stress of prongs, especially in the prong bottom region is crucial for optimizing the stress distribution of QTFs and improving the charge collection efficiency. Besides, for Z-cut QTFs, the lateral crystal prisms inevitably appear on the +X direction sidewalls during the carving process due to the anisotropy of quartz [62,63]. This will lead to unsatisfying straightness of the sidewalls in the +X direction and reduce the electric field component in the X direction. Fortunately, this inevitable property can be weakened by an inclined groove structure. Based on the above shortcomings, the main objectives of this work are summarized as follows: Selecting the appropriate frequency to improve the energy accumulation time; Improving the overall stress of the prongs; and Improving the sidewall quality of the grooves.

In this work, novel 9 kHz T-shaped QTFs with isosceles-trapezoidal grooves are designed and applied to QEPAS system. The stress, charge density, and terminal charge of the QTFs with isosceles-trapezoidal and rectangular grooves are analyzed and simulated to research the electro-elastic properties of the QTFs. Three types of 9 kHz QTFs, characterized as rectangular cross-section prongs, and T-shaped prongs with rectangular and isosceles-trapezoidal grooves, respectively are fabricated and applied to gas detection experiments.

2. The design of QTFs for QEPAS

The schematic diagram of T-shaped QTF with isosceles-trapezoidal grooves is shown in Fig. 1, where X, Y, and Z axes respond to the prongs' width, length, and thickness directions, respectively. l_P, w, and t denote the prong length, width, and thickness, respectively. w_1, w_2, and l_G are the isosceles trapezoid's upper base, lower base, and height, respectively. e is the spacing of prongs. w_M and l_M are the width and length of the hammerhead, respectively.

2.1. The working principle of QEPAS

In photoacoustic spectroscopy, the detected signal S can be expressed as [60]:

$$S = \alpha \frac{PQ}{f_0} \tag{1}$$

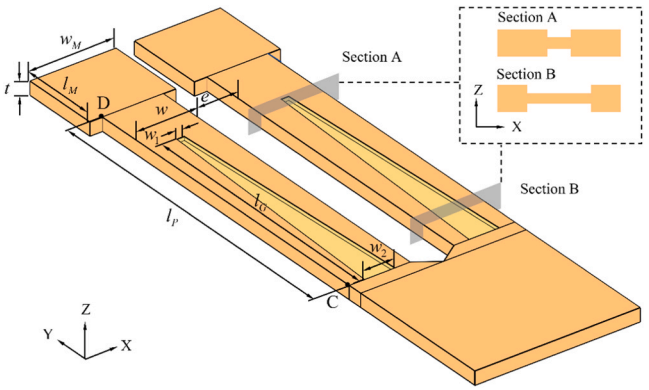

Fig. 1. Schematic diagram of the QTF with grooves.

where α is the absorption coefficient, P is the optical power of the laser, f_0 and Q are the resonance frequency and quality factor of the QTF, respectively. According to Eq. (1), it can be known that reducing the resonant frequency f_0 can effectively improve the detected signal.

The prongs of QTF can be simplified into two independent cantilever beams [64], and the resonance frequency f_0 can be expressed as [65]

$$f_0 = \frac{(\beta_n l)^2}{2\pi}\sqrt{\frac{EI}{\rho A l^4}} = \frac{(\beta_n l)^2}{2\pi}\sqrt{\frac{E}{12\rho}}\frac{w}{l^2} \tag{2}$$

where E, I, ρ, A, w, and l denote Young's modulus, the moment of inertia of the beam cross-section, density of quartz, cross-sectional area, the width along the vibration direction, and the beam length, respectively. $\beta_n l$ is the frequency coefficient for the nth mode, and $\beta_1 l = 1.8751$ for the first model [65]. It can be found from Eq. (2) that $f_0 \propto w/l^2$. Thereby, w and l are vital structure parameters that affect the resonator frequency. In this work, an approximate 9 kHz frequency is selected to obtain a relatively long energy accumulation time of the QEPAS system.

In the QEPAS system, the sound waves push the prongs of QTFs to vibrate in an anti-symmetrical mode, and electric charges can be collected in the prong surfaces due to the positive piezoelectric effect [30,38]. The QTF with high electric charge collection effectivity is expected. The piezoelectric equation can be expressed as [66]

$$\begin{cases} \mathbf{S} = \mathbf{s}^E \cdot \mathbf{T} + \mathbf{d} \cdot \mathbf{E} \\ \mathbf{D} = \mathbf{d}^t \cdot \mathbf{T} + \boldsymbol{\varepsilon}^T \cdot \mathbf{E} \end{cases} \tag{3}$$

where $\mathbf{S}$ and $\mathbf{T}$ are the strain tensor and stress tensor, respectively, $\mathbf{D}$ and $\mathbf{E}$ are the electric displacement vector and the electric field vector, respectively, $\mathbf{d}$ is the piezoelectric strain coefficient tensor, $\mathbf{s}^E$ is the elastic compliance coefficient tensor under a constant electric field, $\boldsymbol{\varepsilon}^T$ is the dielectric coefficient tensor under a constant force, and $\mathbf{d}^t$ is the transposition of $\mathbf{d}$. According to Eq. (3), the surface charges of QTFs can be improved by enhancing the stress of prongs of QTFs.

For a variable section beam with a small taper, the stresses can be expressed as [67]

$$\sigma(y, x) = -\frac{M(y)x}{I} \tag{4}$$

where M is the bending moment, x is the distance from the center axis of the beam. Carving grooves in the upper and lower surfaces of prongs will reduce the moment of inertia I. According to Eq. (4), the stress will increase when the moment of inertia decreases.

2.2. Analysis and simulation of the QTF

In this subsection, the stress, charge density, and terminal charge of the T-shaped QTFs with two types of isosceles-trapezoidal grooves, and normal rectangular grooves are simulated to analyze the electro-elastic properties of the QTFs. In this work, these groove structures are designed to improve the overall stress values and optimize the stress distribution of prongs, which can further enhance the surface charges (in Eq. (3)). Besides, carving grooves can improve the X-direction excitation field strength of prongs. Thereby, the charge collection capacity and the sensitivity of the QEPAS system can be enhanced by the optimized groove structure designs.

2.2.1. QTFs with rectangular grooves

COMSOL Multiphysics is used to analyze the stress distributions of T-shaped QTFs with or without rectangular grooves. Fig. 2 shows the stress distributions along the prong length direction for T-shaped QTFs where $w = 1600$ μm, $l = 8672$ μm, $w_M = 2260$μm, $l_M = 2100$ μm, $t = 350$ μm, and $w_1 = w_2 = 600$ μm ($w_1 = w_2 = 0$ μm). The simulated points are in the CD-segment of Fig. 1. The stress distributions of two T-shaped QTFs (with or without rectangular grooves) are compared. As is shown in Fig. 2, the stress value is large near the prongs' bottom, and the stress

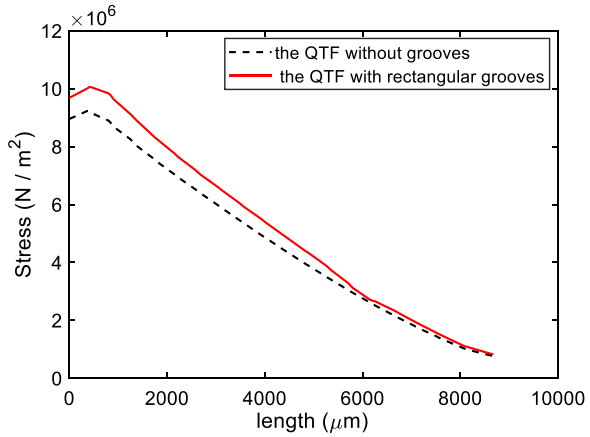

Fig. 2. The distributions of the stress along the prong length direction.

value of one point generally decreases as it is farther away from the bottom regions. Carving grooves mainly affects the stress near the bottom of the prongs, where the stress is relatively large. Comparing the stress distributions of the QTFs, we can find the stress values of the T-shaped QTF with grooves are generally larger than those of the T-shaped QTF without grooves. As shown in Eq. (3), the higher stress leads to a larger electric displacement. Thereby, carving grooves can enhance the surface charge of QTFs and further improve the detection current and sensitivity of the sensing system.

2.2.2. *QTFs with isosceles-trapezoidal grooves*

In this subsection, QTFs with positive and inverted isosceles-trapezoidal grooves are researched, and the schematic structure can be seen in Fig. 3. Compared with the traditional rectangular groove structure, the isosceles-trapezoidal groove structures are proposed to obtain larger overall stresses along the prong length direction. Besides, the isosceles-trapezoidal groove structures have better sidewall quality of the grooves than rectangular groove structures after the wet etching.

The positive and inverted isosceles-trapezoidal groove structures are proposed through different considerations. Fig. 3(a) shows the structure of the QTF with inverted isosceles-trapezoidal grooves. According to the equal strength beam theory[68], the structure of Fig. 3(a) can obtain a more balanced stress distribution and enhance the overall stress. Fig. 3 (b) denotes the QTF with positive isosceles-trapezoidal grooves, which can exacerbate the inhomogeneous character of the stress distribution

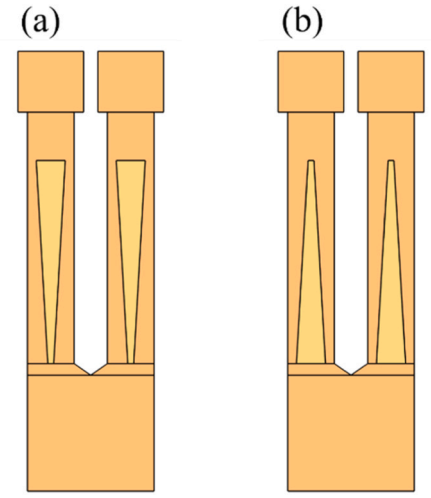

Fig. 3. Schematic structure of the QTFs with isosceles-trapezoidal grooves: (a) the inverted isosceles-trapezoidal grooves; (b) the positive isosceles-trapezoidal grooves.

along the prong length direction, while further improving the stress value near the root area and enhancing the overall stress.

Fig. 4 compares the stress distributions of a normal QTF with rectangular grooves and QTFs with positive and inverted isosceles-trapezoidal grooves where $w = 1600$ μm, $l = 8672$ μm, $w_M = 2260$μm, $l_M = 2100$ μm, and $t = 350$ μm. QTF#T1 (w_1 =200 μm, w_2 =1000 μm) and QTF#T2 (w_1 =1000 μm, w_2 =200 μm) denote the QTF with inverted and positive isosceles-trapezoidal grooves, respectively, and QTF#R ($w_1 = w_2$ =600 μm) represents the QTF with rectangular grooves. As shown in Fig. 4(a)-(c), the stress is large in the region near the bottom of the prongs. It can be seen in Fig. 4(d), that the stress in the prongs with isosceles-trapezoidal grooves is overall greater than that in the prongs with rectangular grooves, and this finding is especially pronounced in the region near the prongs' bottom. Comparing the stress distributions of QTF#T1 and QTF#T2, we can find the stress of QTF#T2 is significantly higher than that of QTF#T1 in the points near the prongs' bottom, while the stress of QTF#T2 is weakly lower than that of QTF#T1 in some points far away from the prongs' bottom. The simulation results reveal the stress distribution of the prongs is optimized by carving isosceles-trapezoidal grooves, and QTF#T2 has better stress distribution due to the large stress near the prongs' bottom area.

The surface charge density distributions of the above three types of QTFs at the corresponding resonator frequency are simulated in Fig. 5. It can be found that the surface charge density of the X-axis electrode is larger, and the surface charge density in the X-axis generally decreases as it is farther away from the bottom regions, which is similar to the stress distribution. As shown in Fig. 5, the lateral surface charge density is relatively large, which is caused by the smaller lateral area compared with the lower and upper surface area. The maximum value of surface charge density in QTF#T1 (3.1E-5C/m^2) and QTF#T2 (4.16E-5C/m^2) is significantly higher than that in QTF#R (2.64E-5C/m^2). This result reveals that the QTF with isosceles-trapezoidal grooves is better at increasing the surface electric charges. To compare the charge collection capability more directly, the terminal charges were calculated by COMSOL Multiphysics. The terminal charges of QTF#R, QTF#T1, and QTF#T2 are 1.1752E-10C, 1.4302E-10C, and 1.5499E-10C, respectively. The results directly indicate that the QTFs with isosceles-trapezoidal grooves (QTF#T1, and QTF#T2) process larger terminal charges than QTF#R, which means outstanding charge collection capability and strong detection electrical signals.

Analyzing the simulations of the stress, surface charge density, and terminal charge, the following main conclusions are obtained: Firstly, the charge collection capability of QTFs can be enhanced by increasing the overall stress of prongs. Secondly, the large values of stress (surface charge density) mainly appear in the region near the prongs' bottom. Thirdly, the grooves of prongs increase the stress and are conducive to optimizing the stress distribution. Finally, the isosceles-trapezoidal grooves QTF have more excellent charge collection capability, especially for QTF#T2 due to the large stress (surface charge density) near the prongs' bottom.

2.2.3. *The sidewall quality of grooves*

For Z-cut quartz, the lateral crystal prisms inevitably appear on the +X direction sidewalls of grooves during the wet etching process due to the different etching speeds of each product surface [69]. The crystal surface angle and corresponding etching speed are shown in Fig. 6, and the specific data can be seen in Reference [70]. The unsatisfying straightness of the sidewalls reduces the electric field component in the X direction. Fortunately, the straightness of the sidewalls can be improved by adjusting the angle of deflection β starting from the Y-axis [71] (the optimized design for QTFs with isosceles-trapezoidal grooves). The definition of the angle of deflection β is shown in Fig. 6(b).

3. Gas detection experiment

In this section, four types of 9 kHz QTFs are fabricated and applied to

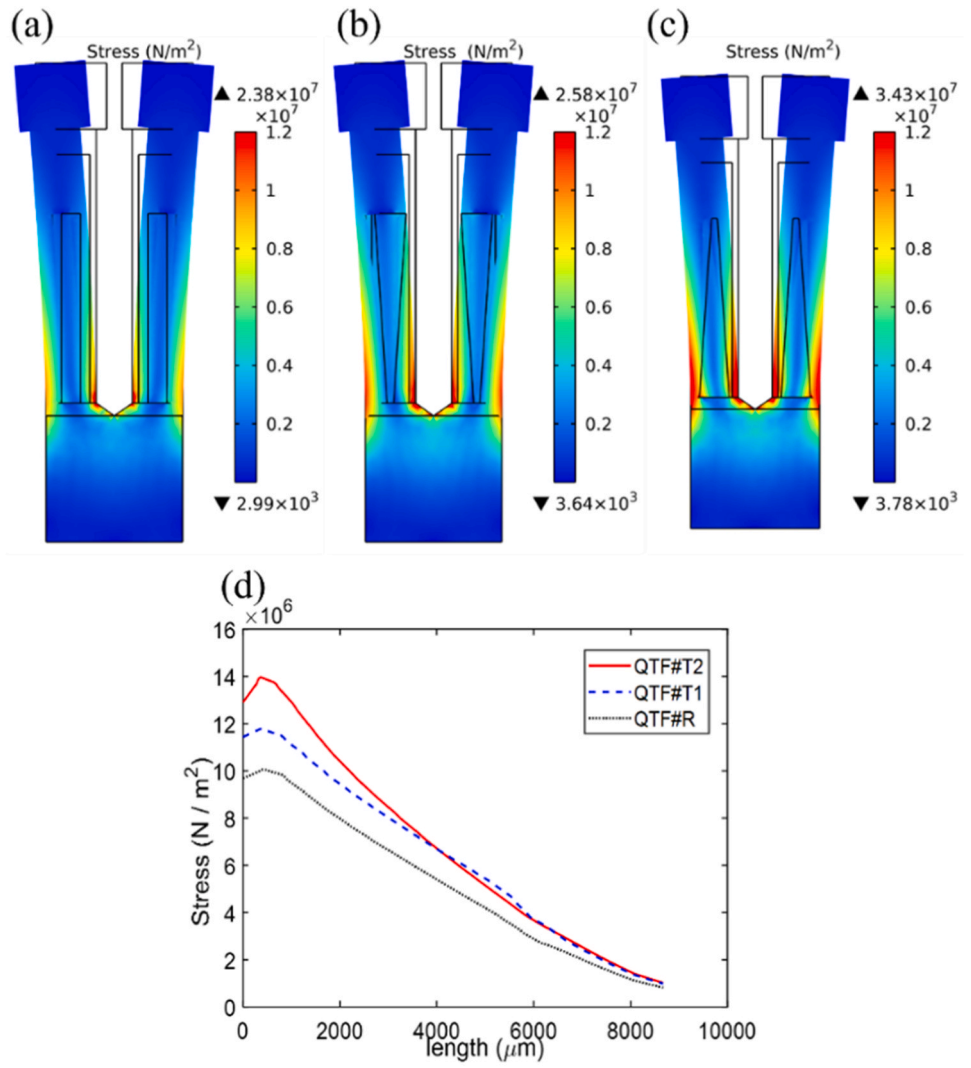

Fig. 4. Stress simulation results of QTFs: (a) QTF#R; (b) QTF#T1; (c) QTF#T2; (d) Stress distributions along the prong length direction for different QTFs.

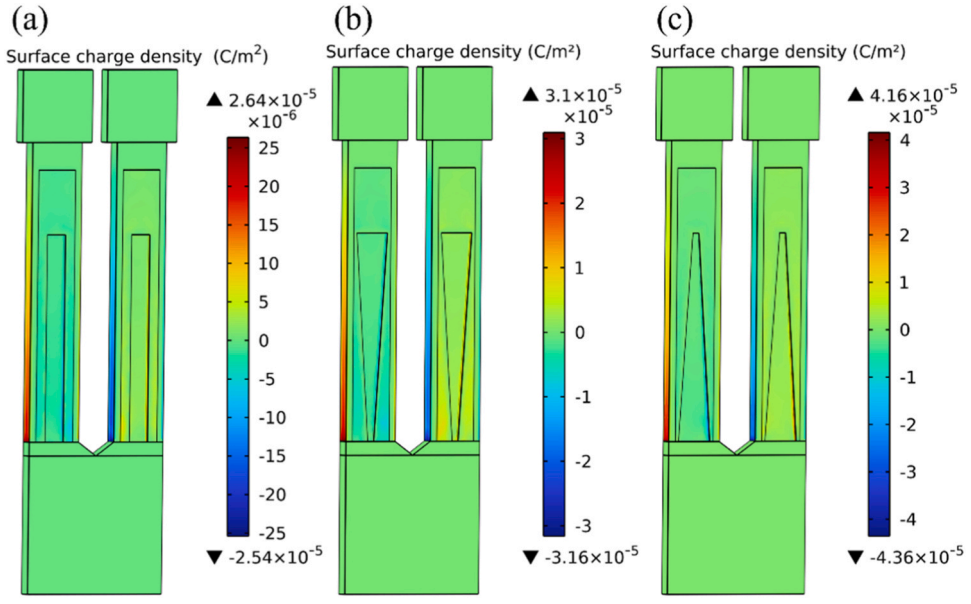

Fig. 5. The surface charge density simulation results of QTFs: (a) QTF#R; (b) QTF#T1; (c) QTF#T2.

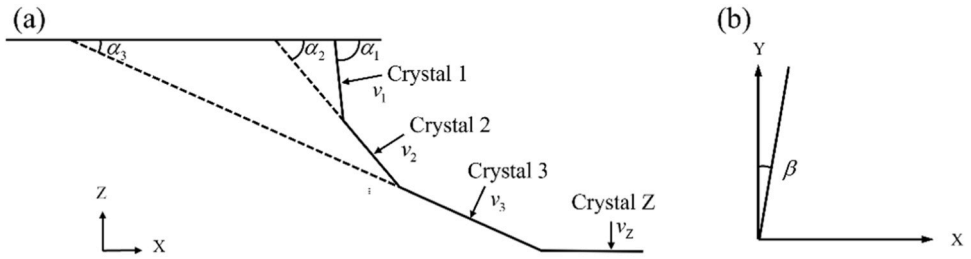

Fig. 6. Schematic diagram: (a) +X direction crystal surface for Z-cut quartz; (b) the angle of deflection β starting from the Y-axis.

gas detection experiments, which are normal QTF with rectangular cross-section prongs (named 'QTF#N'), the T-shaped QTF with rectangular grooves (QTF#R), two types of QTFs with inverted and positive isosceles-trapezoidal grooves (QTF#T1 and QTF#T2). The physical schematic of QTFs can be seen in Fig. 7.

The fabrication process of QTFs in this work can be stated as follows: Firstly, the quart structures of QTFs are fabricated by photolithography and wet etching processes. Then, the surface electrodes of QTFs are obtained by evaporation based on the shadow mask. Comparing the fabrication process of QTF#N, the QTFs of Fig. 7(b)-(d) need carving grooves on the upper and lower surfaces and setting groove internal electrodes. A more detailed fabrication process of QTFs can be in Reference [72].

3.1. Experimental setup

The schematic diagram of the QEPAS sensor setup is shown in Fig. 8. A strong absorption line of acetylene (C_2H_2) located at 1530.37 nm (6534.37 cm^{-1}) was selected. A distributed feedback (DFB) diode laser was employed as the excitation source. Wavelength modulation spectroscopy (WMS) and the second harmonic (2*f*) demodulation techniques have been adopted in this work. The signal generator was used to generate a ramp wave with a low frequency to make the output wavelength of the laser scan through the target absorption line. The lock-in amplifier produced a high-frequency sine wave to modulate the laser, and the modulation frequencies of the laser were set as half of the resonance frequencies ($f_0/2$) of the QTFs. The laser was modulated by these two waves together, and the output laser was collimated by the fiber collimator then incident into the gas cell filled with C_2H_2. The laser beam passed through the gap between the two prongs of the QTF, and a photoacoustic was generated and detected by the QTFs. The detection bandwidth of the used lock-in amplifier was 0.4 Hz.

3.2. Experimental results

The f_0 and Q were measured using the optical excitation method, as shown in Table 1. It can be seen that these QTFs have nearly the same f_0 and a high Q factor greater than 10,000, which is beneficial to improve the QEPAS sensing performance. Compared with Q of QTF#N, Q of QTF#R is improved by 5.4 %, while Q of QTF#T1 (QTF#T2) is decreased by 5.8 % (0.9 %). There are weak differences in Q for different QTFs. Q of QTFs is affected by numerous factors such as structure, surroundings, and fabrication process. Accurately predicting Q of QTFs is challenging and needs in-depth study in the future.

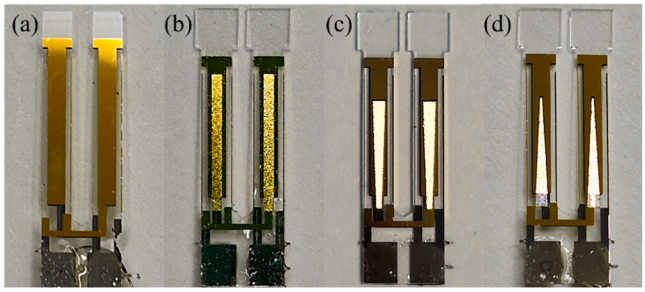

Fig. 7. Physical schematic of the four QTFs: (a) QTF#N; (b) QTF#R; (c) QTF#T1; (d) QTF#T2.

To verify the performance of these four QTFs, 2*f*-QEPAS signals were measured in the C_2H_2-QEPAS sensor mentioned above using 2 % C_2H_2. The obtained results are shown in Fig. 9. To compare the signal peak and SNR values more visually, two bar charts were plotted as shown in Fig. 10. According to Table 1 and Fig. 10, some main conclusions are shown as follows: Comparing QTF#T1, QTF#T2, QTF#R, and QTF#N, we can find T-shaped QTFs with isosceles-trapezoidal grooves (QTF#T1 and QTF#T2) generally have more excellent performance than the T-shaped QTF with rectangular grooves (QTF#R) and normal QTF with rectangular cross-section prongs (QTF#N). QTF#T1 and QTF#T2 weakly affect the Q of QTFs compared to QTF#R, while they significantly reduce the flanking noise and enhance the leaves of SNR and signal peak. The signal peak value of QTF#T2 (QTF#T1) is 1.44 (1.27) times greater than QTF#N, and the SNR value of QTF#T2 (QTF#T1) is 1.85 (1.52) times greater than QTF#N. Furthermore, for T-shaped QTFs with isosceles-trapezoidal grooves (QTF#T1 and QTF#T2), QTF#T2 processes lower flanking noise and higher values of Q, signal peak, and SNR than QTF#T1 due to the excellent charge collection capability, which has been discussed in the simulation subsection.

4. Conclusion

A novel 9 kHz T-shaped QTF with isosceles-trapezoidal grooves is designed and applied to QEPAS gas sensing experiments in this work. Four types of 9 kHz QTFs, characterized as normal rectangular cross-section prongs, T-shaped prongs with rectangular grooves, T-shaped prongs with inverted and positive isosceles-trapezoidal grooves, are fabricated and applied to gas detection experiments. Some main conclusions are shown as follows: The T-shaped QTFs with isosceles-trapezoidal grooves are conducive to optimizing the stress distribution, especially for the structure with positive isosceles-trapezoidal groove (QTF#T2). The T-shaped QTFs with isosceles-trapezoidal grooves have excellent charge collection capability, high electromechanical conversion efficiency, signal peak, and signal-to-noise ratio. The detection performances of T-shaped QTF with isosceles-trapezoidal grooves are superior to normal QTF with rectangular cross-section prongs (QTF#N) and T-shaped QTFs with rectangular grooves (QTF#R), the signal peak and SNR values of QTF#T2 are 1.44 and 1.85 (1.27 and 1.56) times greater than that of QTF#N (QTF#R), respectively.

CRediT authorship contribution statement

Runqiu Wang: Writing – review & editing, Writing – original draft, Methodology, Data curation, Conceptualization. **Feihu Fang:** Writing – review & editing, Writing – original draft, Methodology, Data curation, Conceptualization. **Shengshou Lin:** Writing – review & editing, Investigation, Formal analysis. **Yilü Tao:** Visualization, Validation, Formal

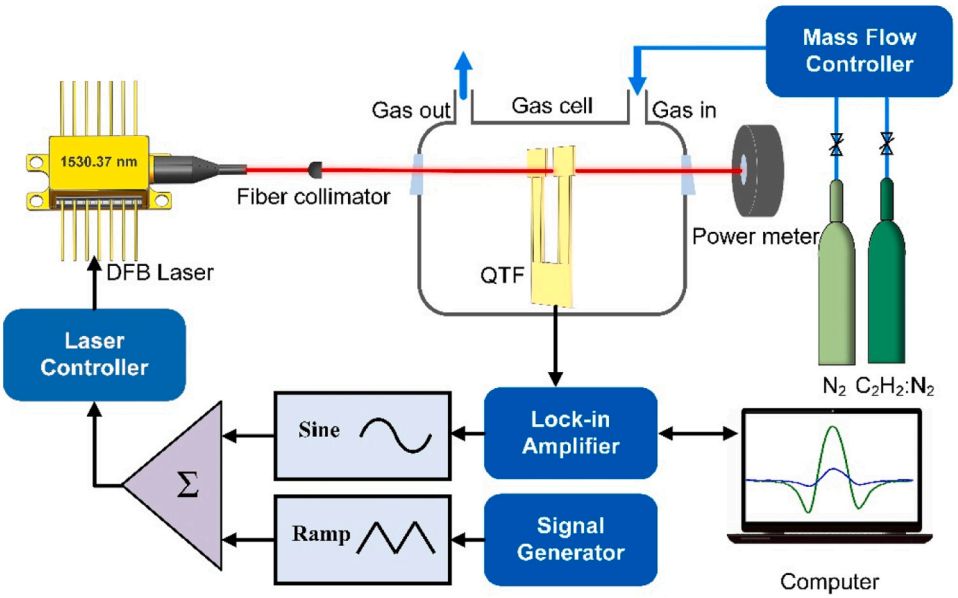

Fig. 8. Schematic diagram of the C_2H_2-QEPAS sensor.

Table 1
The measured f_0 and Q for the four QTFs.

QTF No.	f_0 (Hz)	Q
QTF#N	9014.07	14162
QTF#R	9057.05	14925
QTF#T1	9059.32	13334
QTF#T2	9005.34	14035

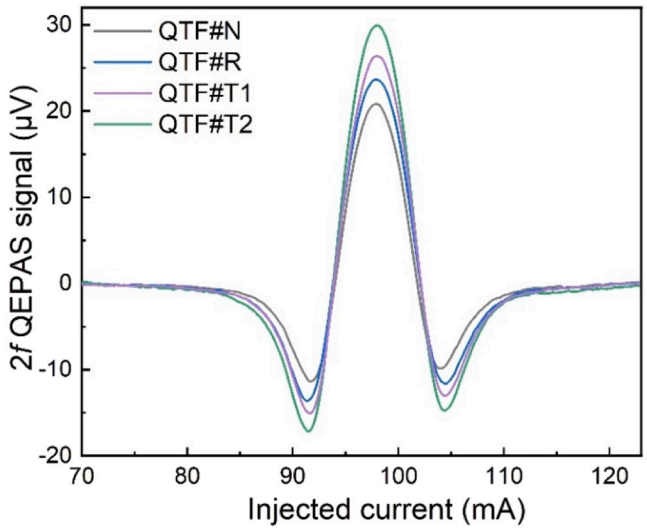

Fig. 9. 2*f* signal of the C_2H_2-QEPAS system with the four different QTFs.

analysis. **Yi Wang:** Visualization, Software, Investigation, Formal analysis. **Dongfang Shao:** Writing – original draft, Software, Formal analysis. **Jinxing Liang:** Writing – review & editing, Supervision, Methodology, Investigation, Formal analysis, Conceptualization. **Yufei Ma:** Writing – review & editing, Supervision, Methodology, Formal analysis, Conceptualization.

Declaration of Competing Interest

The authors declare that they have no known competing financial interests or personal relationships that could have appeared to influence the work reported in this paper.

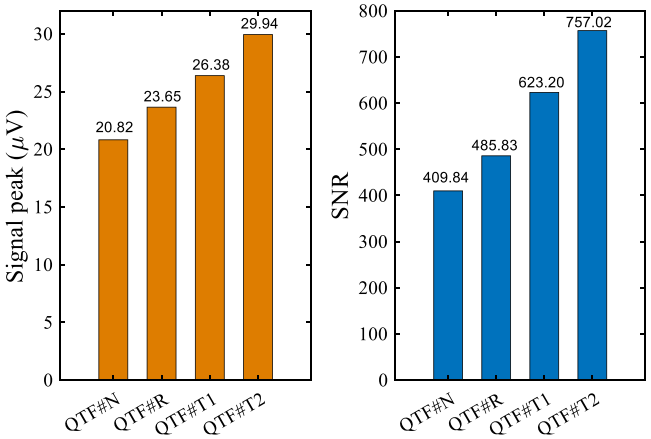

Fig. 10. The experimental results of signal peak and SNR for the different QTFs.

Acknowledgements

Feihu Fang and Runqiu Wang contributed equally to this work. We are grateful for financial supports from the National Natural Science Foundation of China (Grant Nos. 62335006, 62275065, and 62405078)

Supporting Information

Supporting Information is available from the Wiley Online Library or from the author.

Received: ((will be filled in by the editorial staff))
Revised: ((will be filled in by the editorial staff))
Published online: ((will be filled in by the editorial staff))

Data Availability

Data will be made available on request.

References

[1] M. Shao, C. Ji, J. Tan, B. Du, X. Zhao, J. Yu, B. Man, K. Xu, C. Zhang, Z. Li, Ferroelectrically modulate the Fermi level of graphene oxide to enhance SERS response, Opto-Electron. Adv. 6 (11) (2023) 230094.

[2] Y. Wei, C. Shi, Y. Zhang, C. Liu, Y. Tang, P. Ren, C. Wang, Y. Zhang, Z. Liu, Temperature-compensated fiber-optic SPR microfluidic sensor based on micro-nano 3D printing, Opt. Express 31 (23) (2023) 38179–38190.

[3] J.S. Otto, M. Chilcott, A.B. Deb, N. Kjærgaard, Distant RF field sensing with a passive Rydberg-atomic transducer, Appl. Phys. Lett. 123 (14) (2023) 144003.

[4] Y. Wang, J. Zhang, Y. Zheng, Y. Xu, J. Xu, J. Jiao, Y. Su, H.-F. Lü, K. Liang, Brillouin scattering spectrum for liquid detection and applications in oceanography, Opto-Electron. Adv. 6 (1) (2023) 220016.

[5] X. Wang, X. Qiu, M. Liu, F. Liu, M. Li, L. Xue, B. Chen, M. Zhang, P. Xie, Flat soliton microcomb source, Opto-Electron. Sci. 2 (12) (2023) 230024.

[6] Z. Lang, S. Qiao, Y. He, Y. Ma, Disturbance-immune, fast response LITES gas sensor based on out-plane vibration mode employing micro Fabry-Perot cavity with heterodyne phase demodulation, Sens. Actuat. B-Chem. 419 (2024) 136412.

[7] H.H. Liu, D.J.J. Hu, Q.Z. Sun, L. Wei, K.W. Li, C.R. Liao, B.Z. Li, C. Zhao, X.Y. Dong, Y.H. Tang, Y.H. Xiao, G. Keiser, P.P. Shum, Specialty optical fibers for advanced sensing applications, Opto-Electron. Sci. 2 (2) (2023) 220025.

[8] S. Jiang, F. Chen, Y. Zhao, S. Gao, Y. Wang, H.L. Ho, W. Jin, Broadband all-fiber optical phase modulator based on photo-thermal effect in a gas-filled hollow-core fiber, Opto-Electron. Adv. 6 (5) (2023) 220085.

[9] W. Kong, F. Wan, Y. Lei, C. Wang, H. Sun, R. Wang, W. Chen, Dynamic detection of decomposition gases in eco-friendly $C_5F_{10}O$ gas-insulated power equipment by fiber-enhanced raman spectroscopy, Anal. Chem. 96 (38) (2024) 15313–15321.

[10] J. Jing, K. Liu, J. Jiang, T. Xu, S. Wang, T. Liu, Highly sensitive and stable probe refractometer based on configurable plasmonic resonance with a nano-modified fiber core, Opto-Electron. Adv. 6 (6) (2023) 220072.

[11] S. Qiao, Y. He, H. Sun, P. Patimisco, A. Sampaolo, V. Spagnolo, Y. Ma, Ultra-highly sensitive dual gases detection based on photoacoustic spectroscopy by exploiting a long-wave, high-power, wide-tunable, single-longitudinal-mode solid-state laser, Light Sci. Appl. 13 (2024) 100.

[12] C. Lou, J. Dai, Y. Wang, Y. Zhang, Y. Li, X. Liu, Y. Ma, Highly sensitive light-induced thermoelastic spectroscopy oxygen sensor with co-coupling photoelectric and thermoelastic effect of quartz tuning fork, Photoacoustics 31 (2023) 100515.

[13] Y. Liu, S. Qiao, C. Fang, Y. He, H. Sun, J. Liu, Y. Ma, A highly sensitive LITES sensor based on a multi-pass cell with dense spot pattern and a novel quartz tuning fork with low frequency, Opto-Electron. Adv. 7 (3) (2024) 230230.

[14] L. Hu, C. Zheng, M. Zhang, K. Zheng, J. Zheng, Z. Song, X. Li, Y. Zhang, Y. Wang, F. K. Tittel, Long-distance in-situ methane detection using near-infrared light-induced thermo-elastic spectroscopy, Photoacoustics 21 (2021) 100230.

[15] S. Lin, J. Chang, J. Sun, P. Xu, Improvement of the detection sensitivity for tunable diode laser absorption spectroscopy: a review, Front. Phys. 10 (2022) 853966.

[16] H. Sun, Y. He, S. Qiao, Y. Liu, Y. Ma, Highly sensitive and real-simultaneous CH_4/C_2H_2 dual-gas LITES sensor based on Lissajous pattern multi-pass cell, Opto-Electron. Sci. 3 (2024) 240013.

[17] Q. Sun, T. Liu, X. Yu, M. Huang, Non-interference NDIR detection method for mixed gases based on differential elimination, Sens. Actuat. B-Chem. 390 (2023) 133901.

[18] C. Zhang, Y. He, S. Qiao, Y. Liu, Y. Ma, High-sensitivity trace gas detection based on differential Helmholtz photoacoustic cell with dense spot pattern, Photoacoustics 38 (2024) 100634.

[19] W. Chen, S. Qiao, Y. He, J. Zhu, K. Wang, L. Xiao, Y. Ma, Quasi-distributed quartz enhanced photoacoustic spectroscopy sensing based on hollow waveguide micropores, Opt. Lett. 49 (10) (2024) 2765–2768.

[20] Z. Wang, Q. Wang, H. Zhang, S. Borri, I. Galli, A. Sampaolo, P. Patimisco, V. L. Spagnolo, P. De Natale, W. Ren, Doubly resonant sub-ppt photoacoustic gas detection with eight decades dynamic range, Photoacoustics 27 (2022) 100387.

[21] H. Sun, S. Qiao, Y. He, Y. Liu, Y. Ma, Highly sensitive CH_4, C_2H_2 and CO simultaneous measurement LITES sensor based on multi-pass cell with overlapped spots pattern and QTFs with low resonant frequency, Opt. Express 32 (16) (2024) 28183–28194.

[22] M. Gu, J. Chen, Y. Zhang, T. Tan, G. Wang, K. Liu, X. Gao, J. Mei, Portable TDLAS sensor for online monitoring of CO_2 and H_2O using a miniaturized multi-pass cell, Sensors 23 (4) (2023) 2072.

[23] Z. Lang, S. Qiao, Y. Ma, Fabry–Perot-based phase demodulation of heterodyne light-induced thermoelastic spectroscopy, Light.: Adv. Manuf. 4 (3) (2023) 233–242.

[24] R. Wang, T. Huang, J. Mei, G. Wang, K. Liu, R. Kan, W. Chen, X. Gao, Pressure sensing with two-color laser absorption spectroscopy for combustion diagnostics, Opt. Lett. 49 (4) (2024) 1033–1036.

[25] Y. Ma, T. Liang, S. Qiao, X. Liu, Z. Lang, Highly sensitive and fast hydrogen detection based on light-induced thermoelastic spectroscopy, Ultra Sci. 3 (2023) 0024.

[26] M. Hu, D. Zhang, H. Zhang, Y. Liu, W. Wang, Q. Wang, Harmonic phase-sensitive detection for quartz-enhanced photoacoustic-thermoelastic spectroscopy, Photoacoustics 38 (2024) 100633.

[27] S. Qiao, P. Ma, V. Tsepelin, G. Han, J. Liang, W. Ren, H. Zheng, Y. Ma, Super tiny quartz-tuning-fork-based light-induced thermoelastic spectroscopy sensing, Opt. Lett. 48 (2) (2023) 419–422.

[28] A.A. Kosterev, Y.A. Bakhirkin, R.F. Curl, F.K. Tittel, Quartz-enhanced photoacoustic spectroscopy, Opt. Lett. 27 (21) (2002) 1902–1904.

[29] M. Mordmüller, M. Köhring, W. Schade, U. Willer, An electrically and optically cooperated QEPAS device for highly integrated gas sensors, Appl. Phys. B 119 (2015) 111–118.

[30] L. Dong, A.A. Kosterev, D. Thomazy, F.K. Tittel, QEPAS spectrophones: design, optimization, and performance, Appl. Phys. B 100 (2010) 627–635.

[31] A.F.P. Cantatore, G. Menduni, A. Zifarelli, P. Patimisco, M. Gonzalez, H.R. Seren, V. Spagnolo, A. Sampaolo, Lithium niobate–enhanced photoacoustic spectroscopy, Photoacoustics 35 (2024) 100577.

[32] H. Luo, J. Li, H. Lv, J. Xie, C. Wang, H. Lin, R. Zhuang, W. Zhu, Y. Zhong, R. Kan, J. Yu, H. Zheng, Off-plane quartz-enhanced photoacoustic spectroscopy, Opt. Lett. 49 (11) (2024) 3206–3209.

[33] Z. Lang, S. Qiao, T. Liang, Y. He, L. Qi, Y. Ma, Dual-frequency modulated heterodyne quartz-enhanced photoacoustic spectroscopy, Opt. Express 32 (1) (2024) 379–386.

[34] C. Zhang, S. Qiao, Y. He, S. Zhou, Lei Qi, Y. Ma, Differential quartz-enhanced photoacoustic spectroscopy, Appl. Phys. Lett. 122 (24) (2023) 241103.

[35] H. Lin, H. Zheng, B.A.Z. Montano, H. Wu, M. Giglio, A. Sampaolo, P. Patimisco, W. Zhu, Y. Zhong, L. Dong, Ppb-level gas detection using on-beam quartz-enhanced photoacoustic spectroscopy based on a 28 kHz tuning fork, Photoacoustics 25 (2022) 100321.

[36] H. Lv, H. Zheng, Y. Liu, Z. Yang, Q. Wu, H. Lin, B.A.Z. Montano, W. Zhu, J. Yu, R. Kan, Radial-cavity quartz-enhanced photoacoustic spectroscopy, Opt. Lett. 46 (16) (2021) 3917–3920.

[37] J. Hou, X. Liu, Y. Liu, Y. He, W. Zhao, Y. Ma, Highly sensitive CO_2-LITES sensor based on a self-designed low-frequency quartz tuning fork and fiber-coupled MPC, Chin. Opt. Lett. 22 (7) (2024) 073001.

[38] P. Patimisco, A. Sampaolo, L. Dong, F.K. Tittel, V. Spagnolo, Recent advances in quartz enhanced photoacoustic sensing, Appl. Phys. Rev. 5 (1) (2018) 011106.

[39] H. Yi, O. Laurent, S. Schilt, M. Ramonet, X. Gao, L. Dong, W. Chen, Simultaneous monitoring of atmospheric CH_4, N_2O, and H_2O using a single gas sensor based on mid-IR quartz-enhanced photoacoustic spectroscopy, Anal. Chem. 94 (50) (2022) 17522–17532.

[40] Y. Ma, Y. Hu, S. Qiao, Z. Lang, X. Liu, Y. He, V. Spagnolo, Quartz tuning forks resonance frequency matching for laser spectroscopy sensing, Photoacoustics 25 (2022) 100329.

[41] Y. Ma, Y. Liu, Y. He, S. Qiao, H. Sun, Design of multipass cell with dense spot patterns and its performance in a light-induced thermoelastic spectroscopy-based methane sensor, Light Adv. Manuf. 6 (1) (2025), https://doi.org/10.37188/lam.2025.001.

[42] H. Luo, J. Li, H. Lv, J. Xie, C. Wang, H. Lin, R. Zhuang, W. Zhu, Y. Zhong, R. Kan, Off-plane quartz-enhanced photoacoustic spectroscopy, Opt. Lett. 49 (11) (2024) 3206–3209.

[43] P. Patimisco, A. Sampaolo, M. Giglio, S. Dello Russo, V. Mackowiak, H. Rossmadl, A. Cable, F.K. Tittel, V. Spagnolo, Tuning forks with optimized geometries for quartz-enhanced photoacoustic spectroscopy, Opt. Express 27 (2) (2019) 1401–1415.

[44] Y. Ma, Y. He, L. Zhang, X. Yu, J. Zhang, R. Sun, F.K. Tittel, Ultra-high sensitive acetylene detection using quartz-enhanced photoacoustic spectroscopy with a fiber amplified diode laser and a 30.72 kHz quartz tuning fork, Appl. Phys. Lett. 110 (3) (2017) 031107.

[45] S. Qiao, Y. Ma, Y. He, P. Patimisco, A. Sampaolo, V. Spagnolo, Ppt level carbon monoxide detection based on light-induced thermoelastic spectroscopy exploring custom quartz tuning forks and a mid-infrared QCL, Opt. Express 29 (16) (2021) 25100–25108.

[46] T. Liang, S. Qiao, Y. Chen, Y. He, Y. Ma, High-sensitivity methane detection based on QEPAS and H-QEPAS technologies combined with a self-designed 8.7 kHz quartz tuning fork, Photoacoustics 36 (2024) 100592.

[47] Q. Wang, Z. Wang, W. Ren, P. Patimisco, A. Sampaolo, V. Spagnolo, Fiber-ring laser intracavity QEPAS gas sensor using a 7.2 kHz quartz tuning fork, Sens. Actuat. B-Chem. 268 (2018) 512–518.

[48] Y. Ma, S. Qiao, P. Patimisco, A. Sampaolo, Y. Wang, F.K. Tittel, V. Spagnolo, In-plane quartz-enhanced photoacoustic spectroscopy, Appl. Phys. Lett. 116 (6) (2020) 061101.

[49] Z. Shang, S. Li, B. Li, H. Wu, A. Sampaolo, P. Patimisco, V. Spagnolo, L. Dong, Quartz-enhanced photoacoustic NH3 sensor exploiting a large-prong-spacing quartz tuning fork and an optical fiber amplifier for biomedical applications, Photoacoustics 26 (2022) 100363.

[50] Z. Wang, Q. Wang, H. Zhang, S. Borri, I. Galli, A. Sampaolo, P. Patimisco, V. L. Spagnolo, P. De Natale, W. Ren, Doubly resonant sub-ppt photoacoustic gas detection with eight decades dynamic range, Photoacoustics 27 (2022) 100387.

[51] Y. Ma, Y. He, P. Patimisco, A. Sampaolo, S. Qiao, X. Yu, F.K. Tittel, V. Spagnolo, Ultra-high sensitive trace gas detection based on light-induced thermoelastic spectroscopy and a custom quartz tuning fork, Appl. Phys. Lett. 116 (1) (2020) 011103.

[52] P. Patimisco, A. Sampaolo, H. Zheng, L. Dong, F.K. Tittel, V. Spagnolo, Quartz–enhanced photoacoustic spectrophones exploiting custom tuning forks: a review, Adv. Phys.: X 2 (1) (2017) 169–187.

[53] S. Dello Russo, A. Sampaolo, P. Patimisco, G. Menduni, M. Giglio, C. Hoelzl, V. M. Passaro, H. Wu, L. Dong, V. Spagnolo, Quartz-enhanced photoacoustic spectroscopy exploiting low-frequency tuning forks as a tool to measure the vibrational relaxation rate in gas species, Photoacoustics 21 (2021) 100227.

[54] M. Olivieri, M. Giglio, S. Dello Russo, G. Menduni, A. Zifarelli, P. Patimisco, A. Sampaolo, H. Wu, L. Dong, V. Spagnolo, Assessment of vibrational-translational relaxation dynamics of methane isotopologues in a wet-nitrogen matrix through QEPAS, Photoacoustics 31 (2023) 100518.

[55] Z. Shang, H. Wu, S. Li, G. Wang, A. Sampaolo, P. Patimisco, V. Spagnolo, L. Dong, Ppb-level mid-IR quartz-enhanced photoacoustic sensor for sarin simulant detection using a T-shaped tuning fork, Sens. Actuat. B-Chem. 390 (2023) 133937.
[56] Z. Shang, S. Li, B. Li, H. Wu, A. Sampaolo, P. Patimisco, V. Spagnolo, L. Dong, Quartz-enhanced photoacoustic NH3 sensor exploiting a large-prong-spacing quartz tuning fork and an optical fiber amplifier for biomedical applications, Photoacoustics 26 (2022) 100363.
[57] S. Dello Russo, A. Zifarelli, A. Sampaolo, M. Giglio, T. Wei, H. Wu, L. Dong, P. Patimisco, F.K. Tittel, V. Spagnolo, Quartz tuning forks employed as photodetectors in TDLAS sensors, Proc. SPIE (2021) 116930J.
[58] C. Fang, T. Liang, S. Qiao, Y. He, Z. Shen, Y. Ma, Quartz-enhanced photoacoustic spectroscopy sensing using trapezoidal-and round-head quartz tuning forks, Opt. Lett. 49 (3) (2024) 770–773.
[59] Y. Ma, S. Qiao, R. Wang, Y. He, C. Fang, T. Liang, A novel tapered quartz tuning fork-based laser spectroscopy sensing, Appl. Phys. Rev. 11 (4) (2024) 041412.
[60] S. Li, J. Lu, Z. Shang, X. Zeng, Y. Yuan, H. Wu, Y. Pan, A. Sampaolo, P. Patimisco, V. Spagnolo, Compact quartz-enhanced photoacoustic sensor for ppb-level ambient NO2 detection by use of a high-power laser diode and a grooved tuning fork, Photoacoustics 25 (2022) 100325.
[61] S. Li, L. Dong, H. Wu, A. Sampaolo, P. Patimisco, V. Spagnolo, F.K. Tittel, Ppb-level quartz-enhanced photoacoustic detection of carbon monoxide exploiting a surface grooved tuning fork, Anal. Chem. 91 (9) (2019) 5834–5840.
[62] R. Pelle, H. Christer, V.K. Ilia, B. Ylva, Etch rates of crystallographic planes in Z-cut quartz - experiments and simulation, J. Micromech. Micro 8 (1) (1998) 1.
[63] Y. Dong, Y. Zhou, H. Huang, B. Zhang, X. Li, K. Chen, L. Sun, G. Dou, Etching of quartz crystals in liquid phase environment: a review, Nanotech. Precis. Eng. 7 (2) (2024) 025001.
[64] P. Patimisco, A. Sampaolo, L. Dong, M. Giglio, G. Scamarcio, F. Tittel, V. Spagnolo, Analysis of the electro-elastic properties of custom quartz tuning forks for optoacoustic gas sensing, Sens. Actuat. B-Chem. 227 (2016) 539–546.
[65] S.S. Rao, Vibration of Continuous Systems, John Wiley & Sons, Hoboken, 2019.
[66] Z.K. Qin, Piezoelectric Quartz Crystal, National Defense Industry Press, Beijing, 1980.
[67] R.C. Hibbeler, Machanics of Materials, Electronic Industry Press, Beijing, 2006.
[68] H.W. Liu, Mechanics of Materials, Higher Education Press, Beijing, 2017.
[69] J.S. Danel, F. Michel, G. Delapierre, Micromachining of quartz and its application to an acceleration sensor, Sens. Actuators A: Phys. 23 (1) (1990) 971–977.
[70] H. Wang, L. Xie, X. Wu, S. Li, Research on quartz wet etching and flatting process of sidewall arris, Chin. J. Sens. Actuators 22 (2009) 1713–1716.
[71] J. Liang, F. Kohsaka, T. Matsuo, T. Ueda, Wet etched high aspect ratio microstructures on quartz for MEMS applications, IEEJ Trans. Sens. Micro 127 (7) (2007) 337–342.
[72] H. Hida, M. Shikida, K. Fukuzawa, S. Murakami, K. Sato, K. Asaumi, Y. Iriye, K. Sato, Fabrication of a quartz tuning-fork probe with a sharp tip for AFM systems, Sens. Actuators A: Phys. 148 (1) (2008) 311–318.

Feihu Fang is currently pursuing his Ph.D. degree in the school of Instrument Science and Engineering, Southeast University, Nanjing, China. His research interests include developing novel inertial measurement sensors based on quartz material and researching quartz processing technology.

Runqiu Wang received her B.S. degree in optoelectronic information science and engineering from Harbin Institute of technology, China, in 2023. In the same year she pursued a master's degree in physical electronics from Harbin Institute of Technology. Her research interests including trace gas sensing based on quartz-enhanced photoacoustic spectroscopy and light-induced thermoplastic spectroscopy.

Yufei Ma received his PhD degree in physical electronics from Harbin Institute of Technology, China, in 2013. From September 2010 to September 2011, he spent as a visiting scholar at Rice University, USA. Currently, he is a professor at Harbin Institute of Technology, China. He is the winner of National Outstanding Youth Science Fund. His research interests include optical sensors, trace gas detection, laser spectroscopy, solid-state laser and optoelectronics. He has published more than 100 publications and given more than 20 invited presentations at international conferences. He serves as area editor for Elsevier *Photoacoustics* and Wiley *Microwave and Optical Technology Letters,* associate editor for Optica *Optics Express*, SPIE *Optical Engineering* and *Frontiers in Physics*. He also serves as topical editor for CLP *Chinese Optics Letters* and editorial board member for MDPI *Sensors* and *Applied Sciences*.

Jinxing Liang received the Ph. D degree in Measurement Technology from Waseda University, Japan, in 2008. Currently, he is a professor at the School of Instrument Science and Engineering in Southeast University. His research interests include quartz micromachining, quartz resonators and quartz MEMS sensors.